JOURNAL OF MATERIALS SCIENCE **39** (2004) 7009– 7017

Array ordering in dendritic crystals and the influence on crystal perfection

R. E. NAPOLITANO*
Materials & Engineering Physics Program, Ames Laboratory, Materials Science and Engineering Department, Iowa State University, Ames, Iowa 50011, USA
E-mail: ralphn@iastate.edu

D. R. BLACK
Ceramics Division, National Institute of Standards and Technology, Gaithersburg, Maryland 20899, USA

The role of the evolving array structure in the generation of crystal defects within a dendritic grain is investigated. Crystallographic perfection and associated defect structures are characterized using X-ray topography and optical microscopy. Observed structures are compared with quantitative descriptors of array order using a minimum spanning tree (MST) graph analysis. It is observed that the dendritic array structure evolves substantially over a growth length of 25 millimeters while the mosaic nature of the crystal remains relatively constant. The MST edge-length mean and standard deviation parameters are determined to be rather insensitive to differences in the *local* order due to statistical sampling size effects. This sample size dependence of the MST is evaluated with respect to its utility in distinguishing between square and hexagonal order, with varying degrees of superposed random noise. It is found that the MST distinguishing power is dramatically reduced when the sampling size is decreased below approximately 200 points.

1. Introduction

The demand for high performance gas-turbines in aircraft engines and land based generators has driven the development of engine materials which are more resistant to high temperature failure mechanisms. In particular, rotating components, such as turbine blades are subjected to high stresses at temperatures which approach melting. Under these extreme conditions, any crystal imperfections may provide sites for creep voiding and subsequent crack initiation. For these reasons, the high temperature performance of single-crystal components far exceeds the capabilities of their polycrystalline counterparts. Accordingly, the continued development of single-crystal casting processes remains essential to the advancement of gas-turbine technology and, hence, to the ever increasing needs of the transportation and power generation industries.

Due to the highly sensitive dendritic growth morphologies typically observed in superalloy components, the reliable production of single-crystal investment castings remains a challenge. This is particularly true for the intricate shapes that are often required in advanced turbine designs, where the formation of crystal defects is difficult to control. One of the most pervasive problems which arises during single-crystal casting is the development of low-angle boundaries within the dendritic structure and the associated formation of a mosaic structure of subgrains. Although observation of these mosaic patterns is well documented [1–6], there is little understanding of the mechanisms leading to the actual development of local dendrite misorientation. A brief review has been provided previously [7].

It has been shown that the low angle boundary structure in a single-crystal casting is closely related to the shape of the dendritic front envelope as it propagates by various branching events to fill the space of the mold, which may have a complex geometry [7]. Without addressing the mechanism for misorientation development, experimental and computational results have indicated that a self-impinging growth envelope may lead to the formation of a low-angle boundary, when disjointed regions of the dendritic grain become rejoined along a surface. By applying a dendritic connectivity parameter to simulations of the growth of the dendritic network, this *convergence-faulting* was further shown to be more likely under certain types of geometric and thermal constraint, and therefore, related to *both* casting shape and furnace design. Careful design of the casting shape and thermal control system can serve to prevent a disjointed self-impinging interface. However, the degradation of crystal perfection within a given region remains poorly understood, and detailed

*Author to whom all correspondence should be addressed.

descriptors of local order would facilitate numerical modeling schemes and enable more systematic quantitative and statistical representations of experimentally and computationally generated structures.

In the present work, a simple geometry and a well-controlled thermal field are employed to suppress convergence faulting and the formation of low-angle boundaries. Evolution of the dendritic structure is investigated with regard to (i) ordering of the primary array, (ii) degradation of crystalline perfection, and (iii) non-random or directed evolution in crystallographic orientation within the dendritic grain. In addition, we investigate the applicability of the minimum spanning tree (MST) graph parameters to the characterization of *local* order in the two-dimensional array, examining the role of sampling size.

The MST is defined as the graph of minimum total length, containing no closed loops, which connects all points in the 2D array with line segments. The set of segment lengths associated with the MST can be analyzed statistically by directly computing the mean length, m, and the standard deviation, σ, for this population. One of the most noteworthy features of the MST analysis is that random disorder or "noise" can be separated from the underlying order of the array using only these quantities. A perfect 2D array will have a σ value of zero, and the value of m will identify the type of order in the array. As random disorder is introduced to a perfect 2D array, the value of σ increases, and the value of m generally decreases (for most array types) [8]. In the random limit, all arrays converge to a single point in the (m, σ) plane, but the trajectories taken from the perfectly ordered extreme to the completely random extreme are markedly different. Therefore, two different arrays with considerable disorder will lie at different points on the (m, σ) plane due to the differences in the underlying order. Based on these features, the MST construction has been used for the characterization of point distributions in solidification structures [9, 10] and has been employed in other fields where such characterizations are of interest [11–14].

2. Experimental methods

A square-bar single-crystal casting, with a one-centimeter edge length and an overall length of 0.25 m was fabricated from the commercial Ni-based turbine blade alloy, CMSX-4. This specimen was produced using a full scale commercial investment casting process, where it was gang-cast along with several other test bars, all oriented with the long axis of the casting parallel to the translation axis of a cylindrical directional solidification furnace. The square-bar casting used for this study was oriented such that two edges of the square cross-sections were perpendicular to a radial line of the furnace. Hence, two corners of the square cross-section were closer to the center of the furnace than the other two. The commercial casting process used did not afford the opportunity to explicitly *set* the thermal gradient or to measure it directly. However a pouring superheat of 167°C was employed, and the casting was pulled from the furnace at a rate of 0.021 mm/s. These practices result in a high G/V ratio which, coupled with the simple geometry, promote stable primary array growth. Due to increased fluid flow, weakened thermal constraint, and a larger mushy zone, low values of G/V generally lead to the occurrence of crystal defects and an overall breakdown of the primary array structure, as observed by Pollock and Murphy in CMSX-1 at G/V values less than 2.7 K/mm^2 [15]. Images of the casting surface, exhibiting the external (casting surface) structure of the dendritic array, are shown in Fig. 1. Note that no features are observed on the surface that would indicate the presence of such anomalies.

The specimen was serially sectioned in increments of 1 mm, revealing the overall structure of the dendritic array, as shown in Fig. 2 for selected axial locations. Such images were used to generate 2-D maps for the positions of the primary dendrite stems associated with each axial position. From the locations of primary stems, ordering in the primary array was evaluated both globally and locally using a minimum spanning tree (MST) graph construction.

X-ray topography was performed to quantify the deviation from uniform crystallographic orientation in specimen cross-sections, and to examine the variation of this perfection as a function of axial position (growth distance) in the casting. Using the specimen cross-sections obtained from the serial sectioning described above, topographic images were produced using synchrotron radiation, revealing the crystalline integrity of the specimen for each axial position. The topographic analysis was performed using 8 keV synchrotron radiation monochromated with an asymmetrically cut Si{111} double-crystal. Diffraction from the {200} planes was utilized, and topographic diffraction images were recorded on high density film. Image sequences were also obtained using a scintillator-detector and recorded on video tape.

Topographic images were collected over a range of specimen orientations rotated about two orthogonal specimen axes, corresponding to the radial and tangential directions in the directional growth furnace, where the casting was produced. For each axial position, measurements of relative diffracting area were obtained as a function of specimen rotation angle, revealing the relative angular distribution of dendritic grains within the particular cross section. For each series of images, the specimen orientation was varied in 0.5 degree increments, covering the full range of observed nonzero detectable diffracted intensity. All images from these "step-scans" were recorded on video tape. From recorded X-ray images, the integrated grayscale density was quantified as a measure of the total diffracting area for any given cross section and orientation. In addition, the topographic image was recorded on high density film for the orientation in each series corresponding to the maximum diffracting area.

3. Experimental results

Each of the film images shown in Fig. 3 represents an indicated maximum in crystal perfection, at least along the constrained rotation path probed in this experiment. Analysis of the diffraction images from the complete step-scan sequences reveals the variation about these

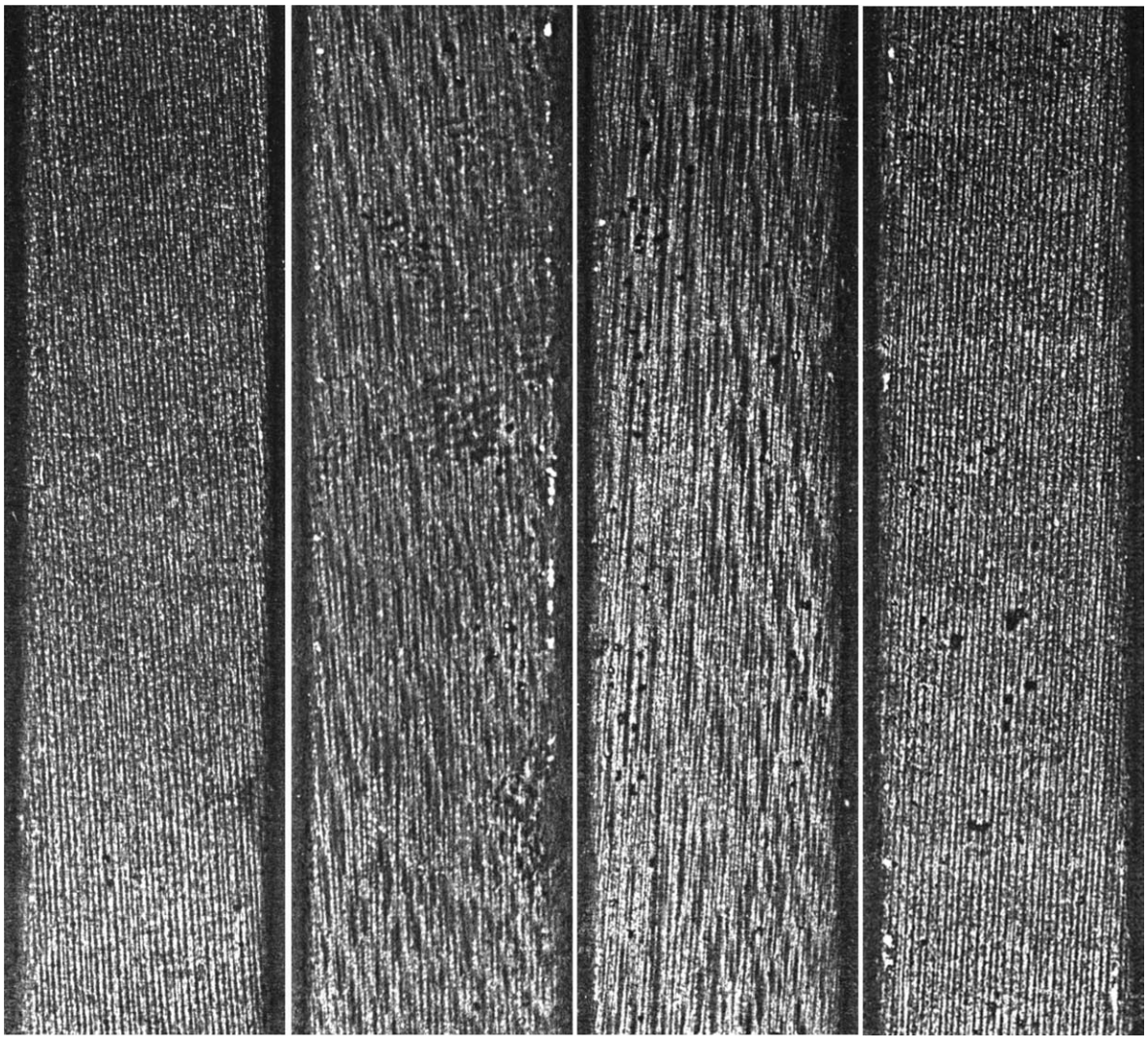

Figure 1 Optical photographs of portions of the casting surfaces, revealing the uniform in-plane primary dendritic pattern on two sides of the casting and out-of-plane growth on the other two sides. For each surface, a length of approximately 5 cm is shown.

maxima, in the integrated diffracted intensity. Such variation with orientation is plotted in Fig. 4, showing the spread in crystallographic orientation at the different axial positions. The sequence in Fig. 3, along with the intensity distributions in Fig. 4, suggest that there is no significant change in crystalline integrity with axial growth distance. However, close inspection of Fig. 2 reveals, qualitatively, that the array is changing substantially over this same growth distance, suggesting that evolution in the structural order of the primary dendritic array may not in itself be sufficient to substantially alter the crystal perfection. Significant and contrary evidence has been reported elsewhere, however, suggesting that the character of the array has a direct effect on the crystal integrity and defect structure [7]. The differentiating factor here is the effect of geometric constraint, dictated by the design of the cast component. In the present case, the role of geometric constraint has been effectively eliminated by the selection of a simple square-bar geometry, resulting in uncompromised thermally constrained dendritic growth, offering little opportunity for the self-impingement required for convergence-fault boundary formation. Indeed, the influence of geometric constraint on the branch-limited propagation of the dendritic array structure has been shown to be a critical factor in the formation of grain defects during solidification [7]. The detailed mechanisms for the evolution of crystal imperfection and associated defects such as low angle grain boundaries, however, is not currently understood, and the relationship between the dendritic array character and degradation in crystal integrity is an ongoing area of investigation. It has been shown recently that dendritic tips may absorb some amount of crystal defect energy to affect a change in the overall growth direction [16]. The conditions which may give rise to this phenomenon are not well established and the transient conditions within an evolving dendritic array are not understood. In the sections that follow, several analyses of the observed dendritic array structure are offered with the intention of providing a basis for comparison with the observed grain defect or "mosaic" structure and a means through which to investigate any relevant correlations.

4. Analysis of dendritic array character

Before examining the array order specifically, it is useful here to briefly discuss the mechanism of branching within the growing dendritic crystal. Clearly, there are two levels of structure important in quantifying

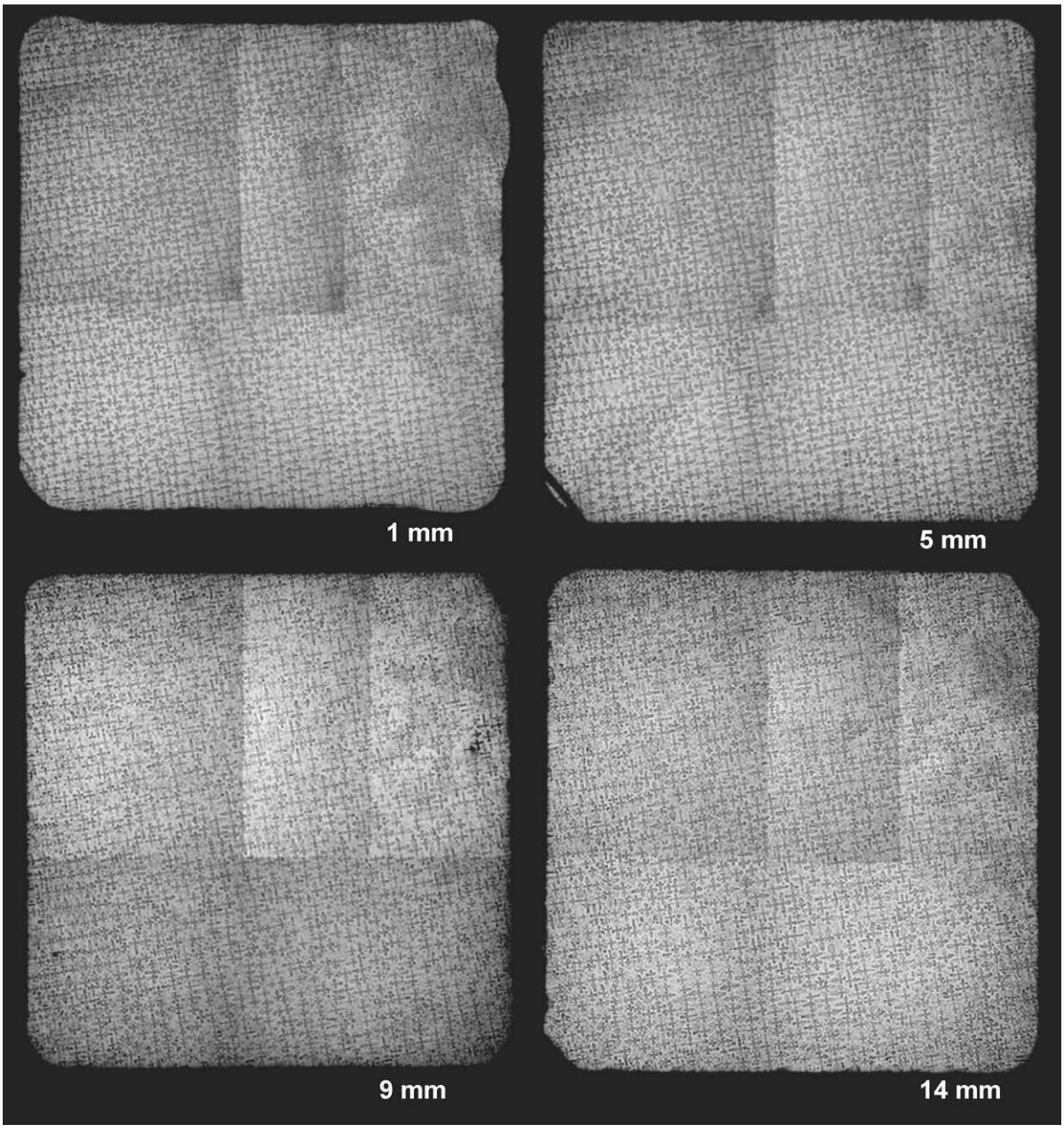

Figure 2 Optical micrographs showing transverse sections of the dendritic arrays observed at selected axial positions, as indicated. The specimen is 10 mm × 10 mm in cross-section. The radial direction of the furnace is vertical in the figure.

the ordering of the dendritic array and the corresponding perfection in the directionally grown crystal. First, there is the overall mosaic pattern indicating various domains of similar crystallographic orientation, as shown in Fig. 3. Second, there is the two-dimensional arrangement of the primary dendritic centers on the growth front. Regarding the former, Fig. 3 suggests that the misorientation and corresponding substructure of low angle boundaries that define the observed mosaic pattern are established very early in the growth process. Indeed, in the specimen examined, the mosaic pattern was established prior to the front reaching the location of the first sectioning plane, located at the base of the specimen, where the cross section first reaches the 13 × 13 mm size. Images from subsequent sectioning planes show that the mosaic pattern remains relatively constant throughout the constant-shape region of the casting. As discussed previously [7], the dendritic branching that occurs in the early stages of growth, when the crystal is growing through a section of rapidly changing cross section, may cause the front to become disjointed. Therefore, convergence faults are likely in this region. Once the growth front moves into the region of constant cross-section, additional substructure is not easily evolved, even though significant changes in the dendritic ordering continue to be observed.

Examination of Fig. 2 reveals dominant secondary dendrite growth in an inward direction from two of the four specimen surfaces. The most dominant of these (the lower surface) is the outward facing surfaces in the casting, where the radial gradient promotes this inward growth. Primary dendrites in this region are aligned in rows, with each primary stem originating from a common branch. Such ordering has been observed and reported previously [5]. As growth proceeds along the length of the specimen, the rows become less well defined. In the following section, the ordering of the dendritic array is evaluated with two primary questions at

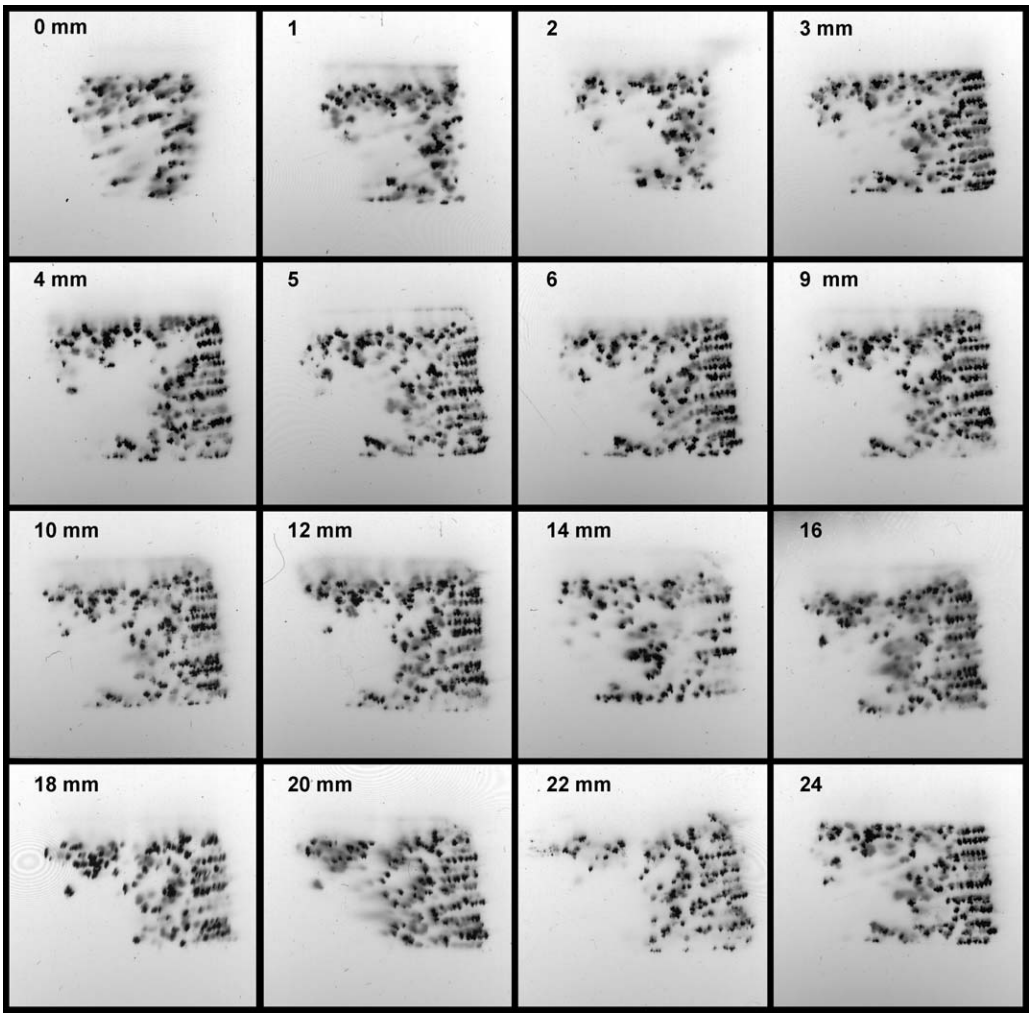

Figure 3 Topographic X-ray images taken approximately at the orientation (about the tangential axis) of maximum diffracted intensity, at the axial position indicated. Diffracting areas (shown dark) indicate regions of identical crystallographic orientation. Here, the radial furnace direction is horizontal.

the forefront. These are: (i) can the mosaic substructure be identified in terms of the 2D ordering in the dendritic array, and (ii) does the evolution of the dendritic order exhibit some systematic drift? To begin to answer these questions, each of the 2D arrays taken from the single crystal specimen was analyzed using a global minimum spanning tree (MST) graph construction [9]. It is assumed that the ordering in the dendritic arrays exhibit either a square or hexagonal structure, and the MST analysis is applied to differentiate between the two, both locally and globally.

As described previously, the MST is defined as the line-segment graph of minimum total length which connects all points in the array without forming any closed loops. For the calculations reported here, the Prim algorithm [8, 17] was employed for MST construction using the arrays observed on each cross-section. MST graphs for selected cross sections are shown in Fig. 5.

The theoretical trajectories from the fully ordered to the fully random arrays in the (m, σ) plane are computed here as a tool for the analysis of the dendritic ordering observed in the single-crystal specimen. For this calculation, varying degrees of disorder are introduced to a perfect square array and a perfect hexagonal array. This is done by assigning a noise vector to each point in the array and displacing each point according to that vector. The noise vectors are distributed randomly in direction and Gaussian in magnitude, where the average displacement is zero. The noise distribution, therefore, is specified uniquely by its standard deviation, σ_{N}. The computed trajectories are shown in Fig. 6, for $n = 500$. Note that all reported values for m, σ, and σ_{N} are normalized by the characteristic spacing, $(A/n)^{1/2}$, where A is the cross-sectional area and n is the statistical sample size (i.e., the number of points in the array).

We now employ these trajectories and consider their utility with regard to comparing MST computations from real arrays for the purpose of distinguishing between the two types of ordering in the dendritic arrays. Because the trajectories for the square and hexagonal arrays lie very close to each other, it is necessary to quantify the repeatability of the MST parameters with respect to the numerically generated random disorder. Furthermore, a real array has a finite number of points and the distinguishing power of the MST parameters will depend on this sample size. In addition, we would like to compare the ordering in different parts of a single array, and the effective use of the MST as an indicator of local structure requires quantification of this size effect.

The issues of repeatability and sample size are examined simultaneously here by generating a series of perfect 2D arrays of both square and hexagonal character,

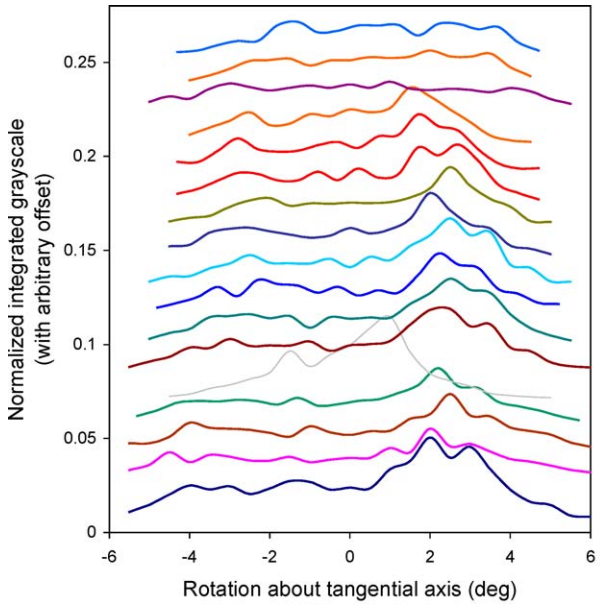

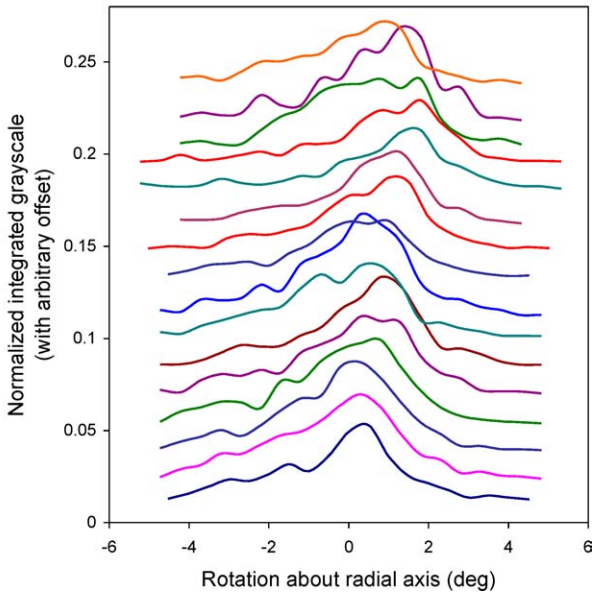

Figure 4 Integrated (areal) diffracted X-ray intensity as a function of specimen orientation. Angular variation is shown about the radial and tangential axes (based on the cylindrical furnace). Plotted distributions are offset sequentially. From bottom to top, curves represent axial positions of 0, 1, 2, 3, 4, 5, 6, 7, 9, 10, 12, 14, 16, 18, 20, 22, and 24 mm, respectively.

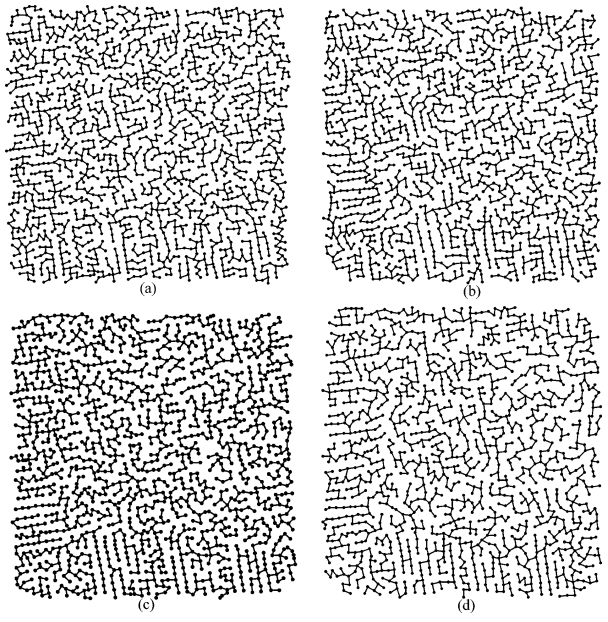

Figure 5 Minimum spanning tree constructions for the dendritic arrays observed on selected cross sections.

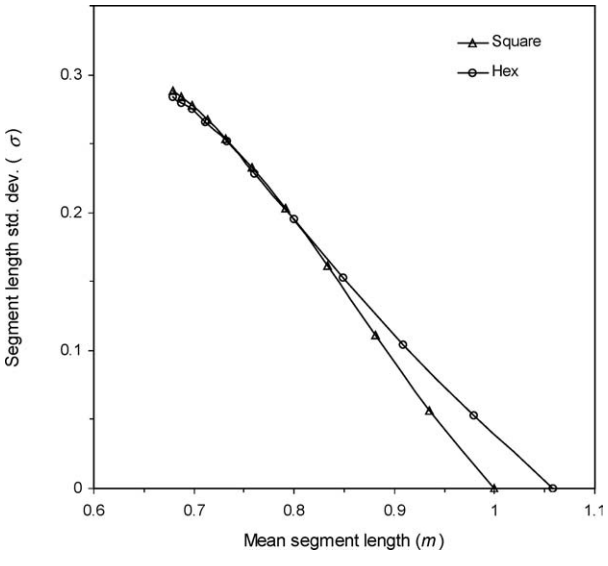

Figure 6 The perfectly ordered to random MST trajectories, computed for square and hexagonal lattices containing 500 points.

with sizes (n) varying from 5 to 2000 points. For each value of n, a series of disordered arrays are generated, using σ_N values that vary from 0 to 100% of the characteristic array spacing. Finally, for each (n, σ_N) pair, twenty different arrays are constructed, each using a different set of numerical seeds for the generation of the random angle and random selection of the displacement magnitude from the set of magnitudes with Gaussian distribution. Typical results for this type of calculation are shown in Fig. 7. Plotted here for a series of n values is the MST mean segment length, m, and the MST segment length standard deviation, σ, for twenty different arrays, each generated using different random number seeds, but all constructed with $\sigma_N = 30\%$. In this way the repeatability is quantified as a function of sample size, also shown in Fig. 7, where the expected interval for the two MST parameters (taken over each set of twenty MST constructions), is plotted as a function of n. This entire procedure was repeated for σ_N values ranging from 0 to 100%.

Examination of Fig. 7 reveals that the variance in the MST parameters decreases very rapidly as n increases from 1 to 100 and appears to stabilize completely between $n = 400$ and $n = 500$. The sample standard deviation (S) for the twenty calculations of the MST parameter σ was computed as a function of disorder. Using the computed mean, m, and the $\pm S$ intervals at this value of n, the repeatability for the trajectories was computed over the full order-disorder range. The result is shown in Fig. 8. Clearly, from this figure, which applies to a sample size of 500 points, the distinguishing power of the MST parameters decreases with increasing disorder. The $\pm S$ intervals begin to overlap approximately at $m = 0.86$ with complete overlap at $m = 0.80$.

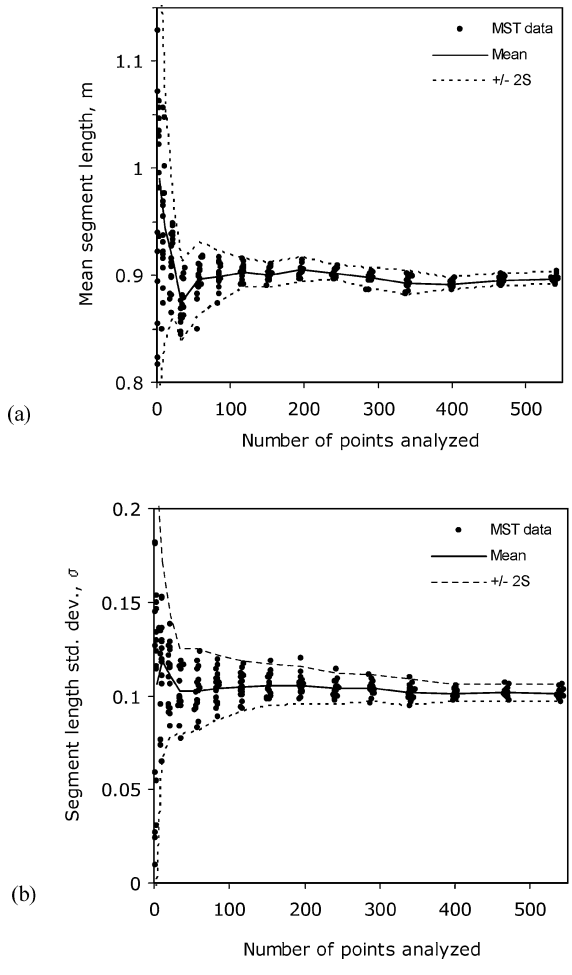

Figure 7 Computational results showing the array-size effect on the MST calculations: (a) MST segment mean and (b) segment standard deviation. Plotted in (c) and (d) are the corresponding curves showing the average values as well as the ± 2s precision band for the calculations in (a) and (b), respectively. Computations based on a square lattice with a superimposed Gaussian noise distribution. For all calculations shown here, a noise distribution standard deviation equal to 30% of the mean MST segment length is implemented.

This range corresponds to a Gaussian disorder between roughly 30 and 40%.

Also shown in Fig. 8 are the MST parameters computed from the dendritic arrays observed on each single-crystal cross section. No systematic variation or *drift* was observed with growth distance. Instead, the parameters appear to vary randomly. Even more notable is the fact that, as a group, the (m, σ) pairs are not located on either of the computed trajectories, although they clearly lie on the square side. This deviation has three likely and related sources: (i) the existence of domains of order, (ii) the existence of domains of orientation, and (iii) the nonuniform areal density of the array. These features are apparent by inspection of the arrays in Fig. 2. Some regions appear to have hexagonal local order while other regions appear to have more of a square array order. Other regions contain linear rows with varying degrees of registry between them. Also, regions of similar order may have a different base orientation. In both of these cases, there exists a substructure of domain boundaries where the influence on the MST is not well characterized. Perhaps most importantly, the local number density is nonuniform. Because the MST is a graph of minimum length, connecting segments will be more concentrated in the more densely packed regions of the array. This implies another type of substructure of high-density clusters or domains with low-density boundaries. Such nonuniform density will bias the parameter m toward a lower value, as observed in Fig. 8.

To examine the local order within the array, we now apply the MST construction to subsets of the arrays. Here we select a circular region on the array, and within this area only, we compute the MST parameters. By rastering this analysis circle over the whole array, a map of the MST parameters can be generated. From Fig. 8, we know that the repeatability of the MST parameters decreases severely as the number of points

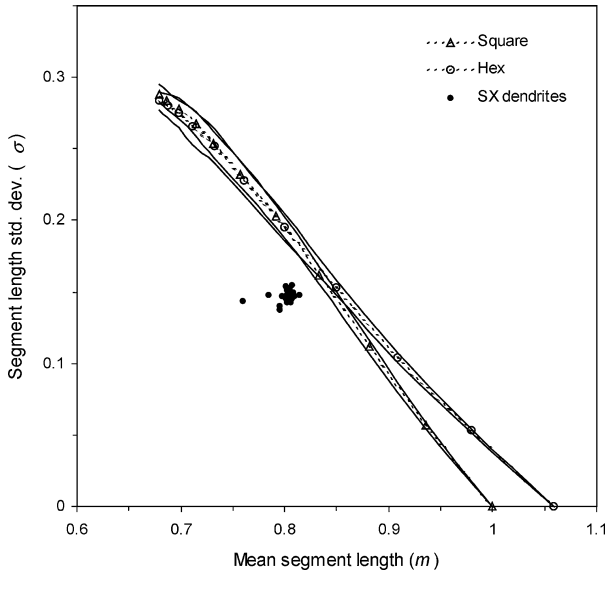

Figure 8 Computed perfect to random minimum spanning tree trajectories for hexagonal and square lattices, showing the uncertainties due to sample-size ($n = 200$).

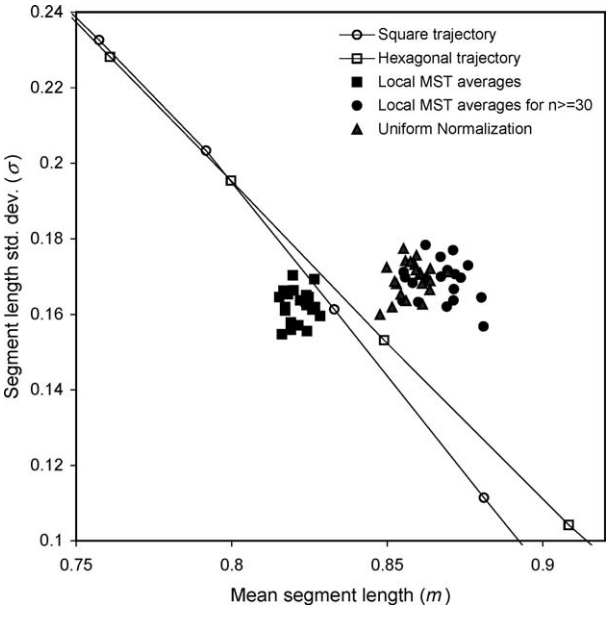

Figure 9 Results from the local minimum spanning tree calculations showing the average local values of m and σ for each specimen cross-section. Also shown are the MST trajectories for the square and hexagonal lattices.

analyzed decreases. Most of this degradation occurs below $n = 30$. Therefore, we select an area for the analysis circle that, on average, contains this number of points. We use a square raster pattern of 900 points on which the analysis circles are centered. If we now plot the average of all local parameters for each cross-section, we observed that these values are very close to the results from the global calculation, with a similar m and a slightly higher σ, lying very close to the square trajectory, as shown in Fig. 9. We now consider a similar calculation of the MST parameters. However, in this second calculation, we do not consider any analysis circle that contains fewer than 30 points. The primary function of this filter is to remove edge effects by ignoring any circular region that intersects the specimen free surface. The resulting cross sectional averages lie at higher m values, as shown in Fig. 9. Finally, we consider a third calculation of the local MST parameters. Here, rather than computing a local normalization length as in the previous case, we compute the normalization length using the entire cross-section and apply it to each of the local MST calculations. We also remove the previously applied filter, since the uniform normalization length will automatically eliminate the edge effects. These results are also plotted in Fig. 9, showing that this third calculation is similar to the second, but that the distribution is somewhat finer and the average parameters are slightly closer to the hexagonal trajectory. This may suggest an underlying hexagonal tendency, however, the data fall in a regime where the ability of the MST trajectories to distinguish between square and hexagonal ordering is substantially

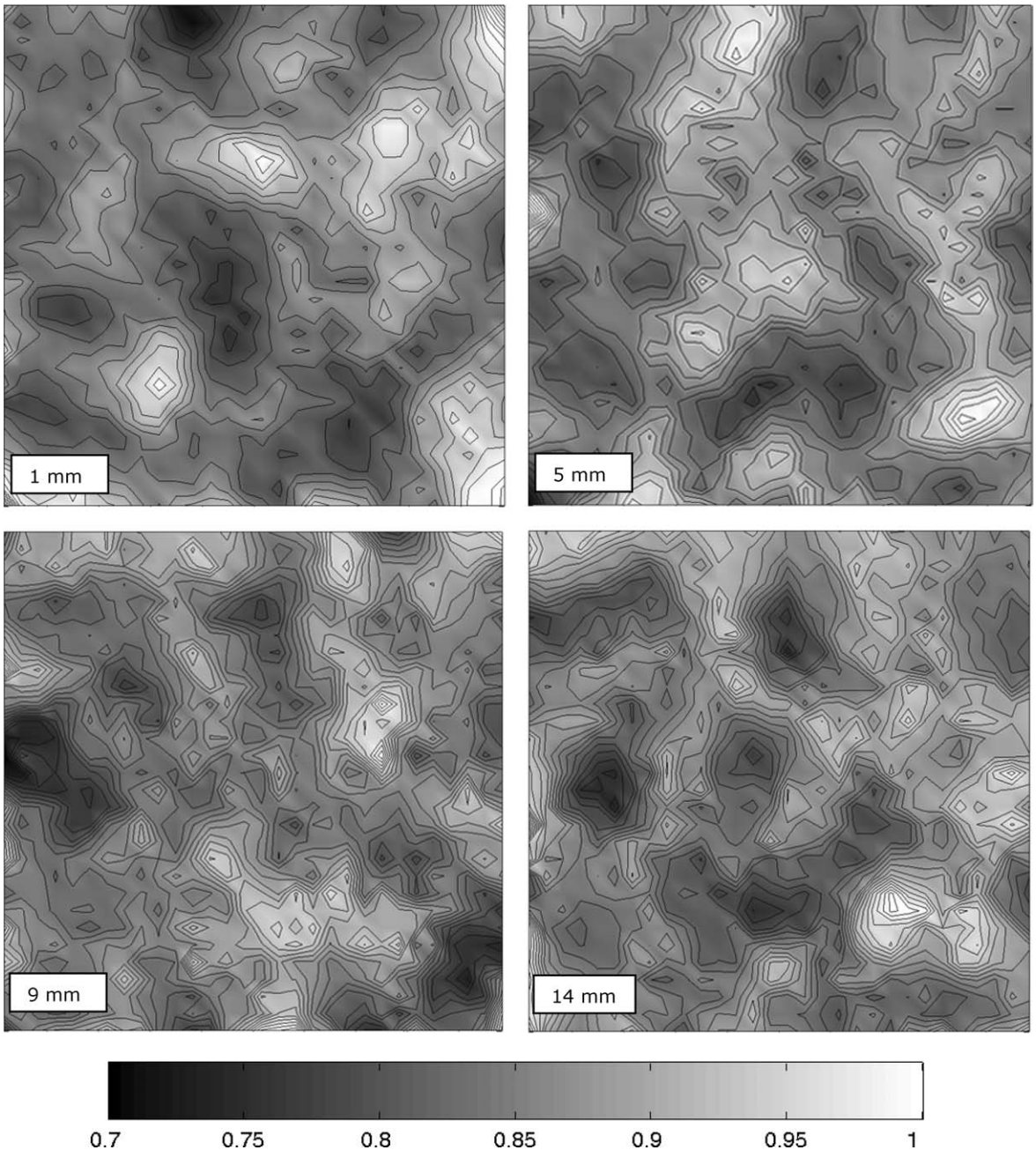

Figure 10 Selected spatial maps of the MST mean segment length, m, computed on a 30×30 grid. At each grid point, the MST is constructed using a circular area of a radius equal to 0.08 times the specimen edge length. Approximately 30 primary dendrite locations are used for each grid point calculation.

diminished. Also noteworthy is that in none of the calculations was any systematic tendency observed with respect to growth distance. Finally, spatial maps of the local MST mean segment length are shown in Fig.10. Correlation with the dendritic morphology and mosaic structure remains unclear.

5. Conclusions

Subgrain mosaic structures form very early in single-crystal dendritic castings, even in very simple geometries. The defect structures remain persistent for very long distances, evidenced here by the fact that they were not observed to dissipate within the examined specimen length of 25 mm.

Although the overall array character is clearly evolving during growth of the dendritic crystal, no systematic change in the structural order of the array was detected using the MST analysis. In addition, while there is a clear correlation between the mosaic patterns observed by X-ray topography and the alignment of primary dendrites into rows, no quantitative relationship between dendritic ordering and crystal integrity was found using the MST parameters.

The minimum spanning tree graph construction may be used to evaluate local order in a 2D array. However, its ability to distinguish between various types of underlying order is dramatically reduced when the number of points is reduced to the range below 200. Because the square and hexagonal MST trajectories lie very close together, the random disorder in the dendritic arrays makes deconvolution of any underlying preferred order particularly difficult. Despite this difficultly, the local MST results weakly suggest an overall tendency for the hexagonal arrangement of primary dendrites.

The MST graph construction and associated calculations are influenced by the presence of a substructure of domains with respect to the type and orientation of the 2D ordering. The influence of these domains and domain boundaries may largely be attributed to nonuniform density. While the simple MST parameters of m and σ were found here to be largely inadequate for either global or local characterization of the dendritic arrays, the uniqueness of the graph construction suggests that more subtle features, such as branch length and segment angular distributions [12] may provide meaningful characterizations that may correlate with crystal integrity.

Acknowledgments

This work was performed within the Ames Laboratory Materials and Engineering Physics Program through the Iowa State University Institute for Physical Research and Technology. The research was made possible by support from the ISU University Research Grant Program and the Office of Basic Energy Science, Division of Materials Science, U.S. Department of Energy, under Contract No. W7405-Eng-82. The X-ray topography experiments were performed at the National Synchrotron Light Source, Brookhaven National Laboratory, supported by the U.S. Department of Energy, Division of Materials Sciences and Division of Chemical Sciences under Contract No.: DE-AC02-98CH10886.

References

1. E. V. AGAPOVA, G. N. PANKIN, V. V. PONOMAREV, V. N. LARIONOV and A. Y. DENISOV, *Izv. Akad. Nauk SSSR, Metally* **2** (1989) 104.
2. U. PAUL, P. R. SAHM and D. GOLDSCHMIDT, *Mater. Sci. Engng.* A **173** (1993) 49.
3. D. BELLET, P. BASTIE, N. SIREDEY, J. LACAZE, A. GEORGE and J. P. MICHEL, in Proc. EUROMAT'89 Conf., edited by H. E. Exner and V. Schumacher (DGM Informations Gellschaft, 1990) p. 413.
4. N. SIREDEY, M. BOUFOUSSI, S. DENIS and J. LACAZE, *J. Cryst. Growth* **130** (1993) 132.
5. M. RAPPAZ and E. BLANK, *ibid.* **74** (1986) 67.
6. R. J. SCHAEFER, D. R. BLACK, M. D. VAUDIN, B. R. MUELLER and A. F. GIAMEI, Solidification Processing 1997: in Proc. 4th Decennial International Conference on Solidification Processing, edited by J. Beech and H. Jones (University of Sheffield, 1997) p. 37.
7. R. E. NAPOLITANO and R. J. SCHAEFER, *J. Mater. Sci.* **35** (2000) 1641.
8. C. DUSSERT, G. RASIGNI, M. RASIGNE, J. PALMARI and A. LLEBARIA, *Phys. Rev.* B **34** (1986) 3528.
9. B. BILLIA, H. JAMGOTCHIAN and H. NGUTEN THI, *Meter. Trans.* **22A** (1991) 3041.
10. *Idem.*, "Growth and Form" (Plenum Press, New York, 1991) p. 211.
11. K. NAKAI, A. KIDERA and M. KANEHISA, *Protein Engng.* **2** (1988) 93.
12. C. DUSSERT, G. RASIGNI, M. RASIGNE, J. PALMARI and A. LLEBARIA, *Z. Physik* D (1989) 41.
13. J. DEVILLERS and J. C. DORE, *Ecotoxical. Environm. Safety* **17** (1989) 227.
14. J. C. DORE, J. GILBERT, E. BIGNON, A. CRASTES DE PAULET, T. OJASOO, M. PONS, J. P. RAYNAUD and J. F. MIQUEL, *J. Med. Chem.* **35** (1992) 573.
15. T. M. POLLOCK and W. H. MURPHY, *Met. Mat. Trans.* **27A** (1996) 1081.
16. V. FERREIRO, J. F. DOUGLAS, J. WARREN and A. KARIM, *Phys. Rev.* E **65** (2002) 051606.
17. R. C. PRIM, *Bell Sys. Tech. J.* **36** (1957) 1389.

Received 27 August 2003
and accepted 20 May 2004